



Small NMR biomolecular sensors

Nan Sun^{a,*}, Yong Liu^b, Ling Qin^c, Hakho Lee^d, Ralph Weissleder^d, Donhee Ham^{c,*}

^a Department of Electrical and Computer Engineering, The University of Texas at Austin, TX 78712, USA

^b IBM T.J. Watson Research Center, Yorktown Heights, NY 10598, USA

^c School of Engineering and Applied Sciences, Harvard University, Cambridge, MA 02138, USA

^d Center for Systems Biology, Massachusetts General Hospital, Harvard Medical School, Boston, MA 02114, USA

ARTICLE INFO

Article history:

Available online 21 March 2013

Keywords:

Nuclear magnetic resonance (NMR)
Radio-frequency (RF) integrated circuits
CMOS integrated circuits
Biomolecular sensing
Biosensor
Magnetic particles

ABSTRACT

By combining the physics of nuclear magnetic resonance (NMR) and silicon radio-frequency (RF) integrated circuits, we recently created progressively smaller NMR systems, which we originally reported in Refs. [1–4]. Our strategy for NMR system miniaturization proved effective, culminating in the smallest prototype [3,4] that weighs 0.1 kg and can be held at the palm of the hand. These small, low-cost NMR systems can be useful as biomolecular sensors in the personalized medicine setting, and we demonstrated their ability to detect proteins, compounds, and human cancer cells. The present paper, which is not a new technical contribution, reviews these developments.

© 2013 Elsevier Ltd. All rights reserved.

1. Introduction

NMR is the resonant energy exchange between RF magnetic fields and atomic nuclear spins subjected to static magnetic fields. It has served as a powerful means to examine the fundamental physics of atomic nuclei, to analyze molecular structures, and to probe properties of materials [5–7]. It has also had prodigious impact in medicine and technology with such applications as medical imaging [8], biomolecular sensing [9,10], well logging [11], and product quality control [12]. Most NMR instruments extant are bulky, heavy, and expensive. If they can be miniaturized, the scope of NMR applications can be broadened. For example, small, low-cost NMR biomolecular sensors would be relevant to medical diagnostics in the context of personalized medicine. Recently, we have developed such miniature NMR systems, aimed in particular at biomolecular sensing, which we originally reported in [1–4]. The present paper seeks to review these developments.

Magnets, coils, and RF transceivers are three key components of NMR systems. The magnet produces static magnetic fields that polarize nuclear spins. The coil and RF transceiver are used to generate excitation RF magnetic fields and also to monitor the dynamics of the nuclear spins. By far the largest component in typical NMR systems is the magnet. A physically larger magnet (even for the same static field strength) is usually preferred, as it tends to produce a more homogeneous static field, which then can excite

a larger volume of sample (as we will detail in Section 2), yielding a stronger NMR signal. The large magnets lead to the traditionally bulky NMR instrumentation.

In creating our miniature systems, we used substantially smaller magnets, and to detect the NMR signal significantly weakened due to the use of the small magnets, we developed highly-sensitive RF transceivers. In addition, these RF transceivers were implemented as CMOS integrated circuits (in conventional systems where large and expensive magnets dominate the system size and cost, such integrated transceiver would not be as meaningful from the cost and size points of view). Fig. 1 shows our 1st, 2-kg, NMR prototype [1,2], which is 60 times lighter and 40 times smaller than a 120-kg state-of-the-art commercial benchtop NMR system [13]. It uses a magnet the size of a fist (this small magnet and the large magnet of the commercial system produce similar static fields of ~0.5 T). The RF transceiver was partially integrated in a 0.18- μm CMOS chip. The in-house fabricated planar microcoil has a quality factor, Q , of 16.

Fig. 2 shows our 2nd NMR prototype [3,4], which integrates the planar coil and RF transceiver in the same CMOS 0.18- μm chip. The RF transceiver has a higher level of integration than the 1st prototype, and achieves a high-enough sensitivity to cope with the signal-to-noise reduction caused by the lossy on-chip coil with a Q of only 1.9. This ‘1-chip’ NMR system, which operates with the same magnet as in the 1st prototype, manipulates nuclear spins on the CMOS chip in its coil region, enabling lab-on-a-chip experiments.

Our 3rd NMR prototype (Fig. 3) [3,4], which uses an even smaller magnet, weighs only 0.1 kg; it is the smallest complete NMR system ever to the best of our knowledge. This system, which

* Corresponding authors.

E-mail addresses: nansun@mail.utexas.edu (N. Sun), donhee@seas.harvard.edu (D. Ham).

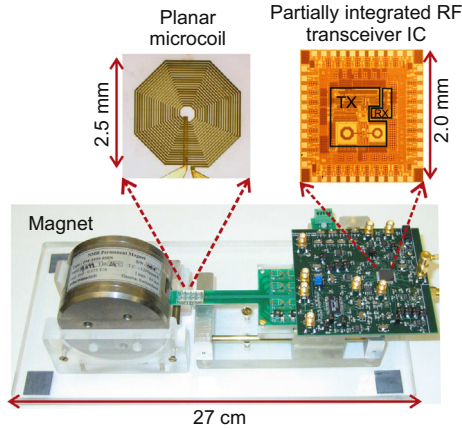


Fig. 1. Our 1st miniature NMR system (figure adapted from [1,2]).

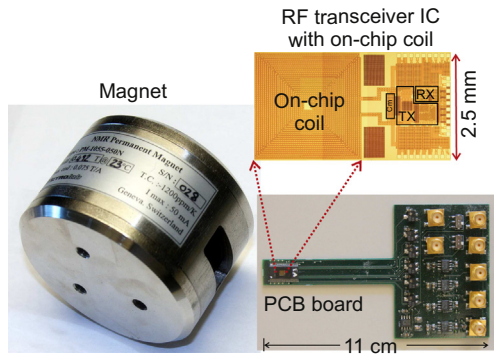


Fig. 2. Our 2nd, '1-chip,' NMR system (figure adapted from [3,4]).

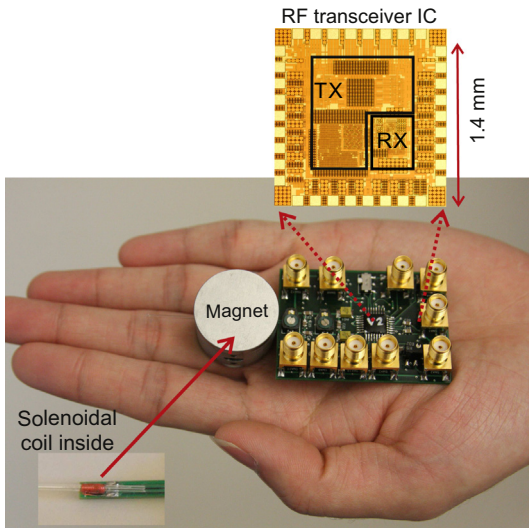


Fig. 3. Our 3rd, 'palm,' NMR system (figure adapted from [3,4]).

can be held at the palm of hand, is 1200 times lighter and 1200 times smaller than the aforementioned commercial system. As the NMR signal is lowered due to the use of the small magnet, this 'palm' system uses a high-quality ($Q = 28$) solenoidal coil in order not to further weaken the signal, while employing the high-performance RF transceiver IC, as in the 2nd prototype.

In what follows, we will review the design of these miniature NMR systems and biomolecular detection experiments with them. But let us get started with the basic NMR review first.

2. NMR and NMR-based biomolecular sensing

Although NMR is a well-established subject [5,6], we here review its basics and its application to biomolecular sensing to the extent pertinent to our work in hopes of making this paper self-contained for this journal's readership. NMR experiments can be done with various atomic nuclei. We will consider protons, the nuclei of hydrogen atoms (^1H), as all our experiments concern ^1H NMR with water.

2.1. Protons in static magnetic field

Due to spin, the proton has an intrinsic magnetic moment $\vec{m} = \gamma \vec{S}$ where $\gamma \sim 42.6 \text{ MHz/T}$ is the proton gyromagnetic ratio and \vec{S} is the spin angular momentum. The single-proton Hamiltonian in an external static magnetic field $\vec{B}_0 = B_0 \hat{z}$ (\hat{z} : unit vector along z -axis) is its potential energy: $H = -\vec{m} \cdot \vec{B}_0 = -\gamma \vec{S} \cdot B_0 \hat{z} = -\gamma B_0 S_z = -\omega_0 S_z$, where $\omega_0 \equiv \gamma B_0$ is the angular Larmor frequency. S_z has two eigenstates; the 'spin-up' state with eigenvalue $\hbar/2$ and the 'spin-down' state with eigenvalue $-\hbar/2$, where $\hbar \equiv h/(2\pi)$ (h : Planck constant). Therefore, the spin-up and -down states are the eigenstates of the Hamiltonian as well, with energies $-\hbar\omega_0/2$ and $\hbar\omega_0/2$, respectively.

A large number of ^1H proton magnetic moments in a macroscopic sample, such as water, in $B_0 \hat{z}$ and at ambient temperature T will reach thermal equilibrium, where the proton population ratio between the spin-up and -down states will be $e^{\hbar\omega_0/(2kT)}/e^{-\hbar\omega_0/(2kT)}$ (k : Boltzmann constant). Since $\hbar\omega_0 \ll kT$ at room temperature and with typical B_0 values, this ratio is only very slightly larger than 1. Nonetheless, with a typical macroscopic sample containing a large number of protons, the absolute difference in populations is still considerable, producing an appreciable net macroscopic magnetic moment \vec{M} along the positive z -axis (Fig. 4a). Specifically, $\vec{M} = M_0 \hat{z}$ with

$$M_0 = \gamma \sum_j S_{j,z} = N\gamma \frac{\hbar/2 \cdot e^{\hbar\omega_0/2kT} - \hbar/2 \cdot e^{-\hbar\omega_0/2kT}}{e^{-\hbar\omega_0/2kT} + e^{\hbar\omega_0/2kT}} \approx \frac{N\gamma^2 \hbar^2 B_0}{4kT}, \quad (1)$$

where N is the total number of protons, the summation runs over all protons, and the last expression is an approximation using $\hbar\omega_0 \ll kT$. A stronger B_0 and a larger sample size (larger N) yield a stronger M_0 .

2.2. Excitation mode – NMR and Rabi oscillation

Once the sample attains the equilibrium macroscopic magnetic moment $M_0 \hat{z}$ in the static field $B_0 \hat{z}$, let a perturbing RF magnetic field of angular frequency ω and amplitude B_1 be applied to the sample perpendicularly to $B_0 \hat{z}$. Without loss of generality, x -axis may be assigned to the direction of the RF field, which then can be written as $\vec{B}_1(t) = \hat{x} B_1 \cos(\omega t)$. This RF field can be generated by wrapping a coil around the sample and transmitting an RF current into the coil (Fig. 4b). The resulting time evolution of the macroscopic magnetic moment $\vec{M}(t)$ can be described by the following equation of motion:

$$\frac{d\vec{M}(t)}{dt} = \gamma \vec{M}(t) \times [B_0 \hat{z} + B_1 \cos(\omega t) \hat{x}], \quad (2)$$

which states that the torque $\vec{M}(t) \times [B_0 \hat{z} + B_1(t) \hat{x}]$ exerted on $\vec{M}(t)$ is equal to the time derivative of the macroscopic angular momentum

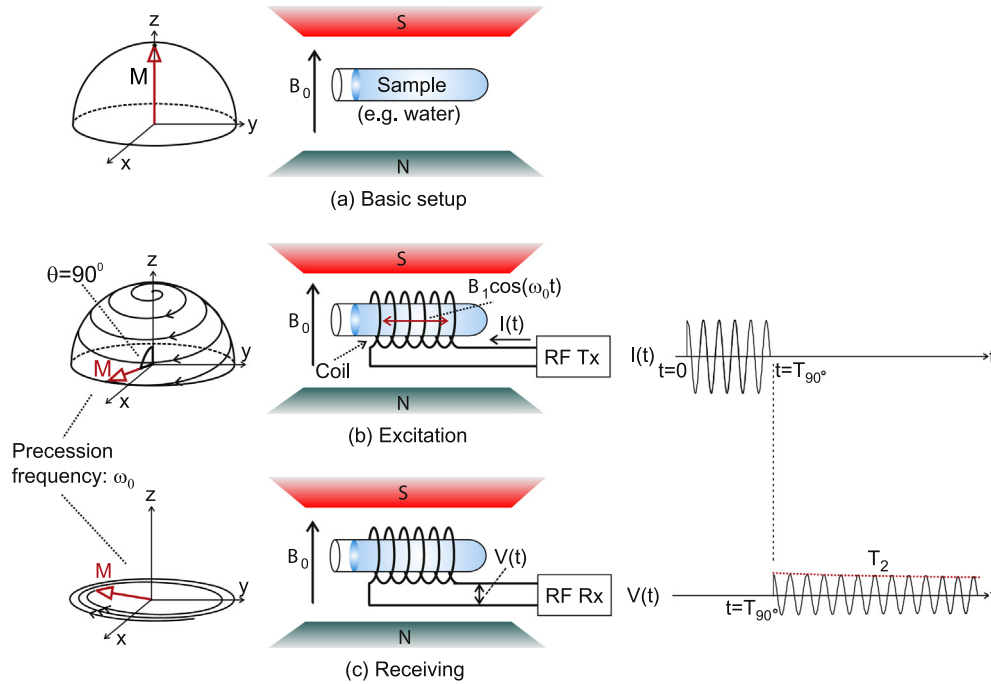


Fig. 4. NMR basics.

$\vec{M}(t)/\gamma$. Solving Eq. (2) is straightforward. We only discuss the result.

If the excitation frequency ω is different from the Larmor frequency ω_0 , the perturbation is not effective, and $\vec{M}(t)$ remains to be $M_0\hat{z}$. If ω closes onto ω_0 , $\vec{M}(t)$ absorbs energy from the RF magnetic field, and uses it to increase its potential energy by increasing the angle θ it makes with the static field $B_0\hat{z}$ (Fig. 4b). If the RF perturbation at $\omega = \omega_0$ continues, θ keeps increasing to the maximum, π , with $\vec{M}(t)$ attaining the maximum potential energy, then, θ decreases back to 0 with $\vec{M}(t)$ releasing its potential energy back to the RF field, and then, θ grows again, and so on so forth. This resonant energy exchange between the RF field and $\vec{M}(t)$ is NMR. The oscillation of θ occurs at frequency $\omega_1 = \gamma B_1/2$ (Rabi oscillation).

In addition to the Rabi oscillation that periodically modulates the z-component of $\vec{M}(t)$ at frequency ω_1 , $\vec{M}(t)$ also undergoes precession about the z-axis due to the torque the static field $B_0\hat{z}$ exerts, thus its x and y components are also periodically modulated. This precession motion, which does not alter the potential energy with respect to the static $B_0\hat{z}$ field, occurs at ω_0 . Overall, $\vec{M}(t)$ will exhibit a spiral downward (or upward) motion (Fig. 4b). The downward/upward motion of $\vec{M}(t)$ (change of θ) is normally much slower than the spiral motion (precession), as typically $B_1 \ll B_0$ thus $\omega_1 \ll \omega_0$.

The resonant excitation frequency ω_0 corresponds to the energy splitting between the spin-up and -down states. In fact, the dynamics above can be obtained by using the standard quantum mechanical treatment instead of using the classical Eq. (2); one can exactly solve the time-dependent Schrödinger equation, with the single-spin Hamiltonian $H(t) = -\gamma \vec{S} \cdot [B_0\hat{z} + B_1 \cos(\omega t)\hat{x}] = -\omega_0 S_z - 2\omega_1 \cos(\omega t) S_x$, and put together the solution with thermal distribution consideration.

2.3. Reception mode

After a certain duration of the resonant RF excitation ($\omega = \omega_0$), which tips \vec{M} away from the z-axis to a certain angle $\theta = \theta_0$, the coil is switched from the RF transmitter to the RF receiver (Fig. 4c). This switchover terminates the resonant energy exchange process, and

θ is now kept at θ_0 for a while (\vec{M} will eventually relax back to the equilibrium position of $\theta = 0$, but this is a leisurely process taking several seconds, which is far slower than the faster dynamics considered here), but the ω_0 -precession persists. The consequent variation of the magnetic flux across the coil induces a sinusoidal voltage $V(t)$ with frequency ω_0 across the coil, which is picked up by the RF receiver. We will call $V(t)$ NMR signal (although NMR actually occurs during the excitation mode). Typically, to maximize the amplitude of $V(t)$ in the reception mode, the excitation mode is terminated when $\theta_0 = 90^\circ$ with \vec{M} on the xy plane; as the Rabi oscillation frequency is $\omega_1 = \gamma B_1/2$, the duration of the excitation mode to change θ from 0 to 90° is given by

$$T_{90^\circ} = \frac{\pi}{\gamma B_1}. \quad (3)$$

$V(t)$ decays exponentially with a characteristic time called T_2 (Fig. 4c). This damping is not due to, and occurs faster than, the energy relaxation parenthetically mentioned shortly before. It is caused by random interactions among the proton spins (spin-spin interactions), which perturbs the ω_0 -precession of each proton spin, causing its phase to undergo a random walk process [14–16]. Consequently, the precessions of the large number of protons grow out of phase with time, rendering the vector sum \vec{M} exponentially decay, leading to the damped $V(t)$. For pure water at room temperature, $T_2 \sim 1$ s. This damping is typically very slow as compared to the spin precession; for example, for $\omega_0 \approx 21$ MHz ($B_0 \approx 0.5$ T), 10^7 precession cycles occur before $V(t)$ decays appreciably.

2.4. NMR-based biomolecular sensing

Consider a biological sample containing a large number of water molecules (thus a large number of ^1H protons). To detect particular proteins in the sample, magnetic nanoparticles coated with antibodies that can specifically bind to the target proteins are introduced into the sample (Fig. 5) [9]. In the absence of the target proteins (Fig. 5b), the magnetic particles stay mono dispersed. These magnetic particles incessantly move around due to Brownian motion, producing fluctuating magnetic fields. These disturb

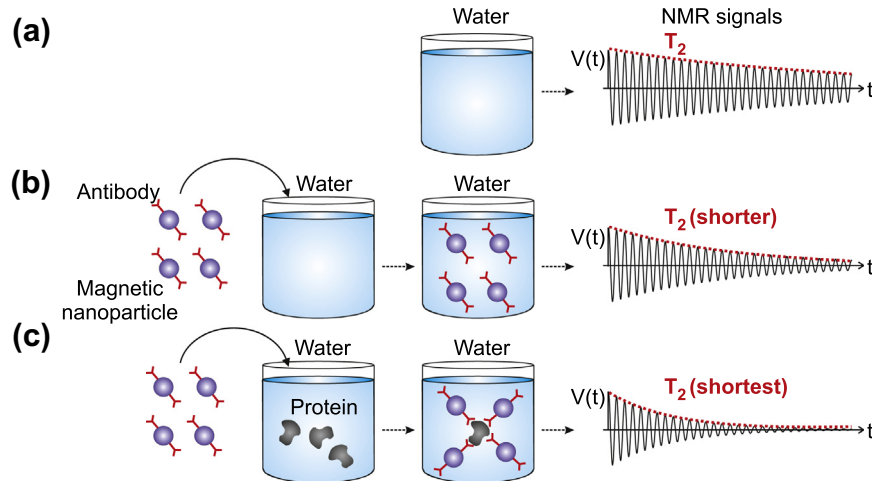


Fig. 5. NMR-based biomolecular detection [9].

precessions of the proton spins, increasing their phase noise beyond that due to the basic spin–spin interactions. Therefore, the phase coherence is lost at a higher rate, reducing T_2 . In the presence of target proteins (Fig. 5c), the magnetic particles assemble into local clusters, which are even more efficient in accelerating the dephasing of ^1H proton precessions, yielding an even smaller T_2 . In summary, by monitoring T_2 of ^1H NMR signal, target proteins can be detected [9].

2.5. Spin echo technique

This biosensing strategy rests on T_2 measurement. We have so far assumed a uniform static field B_0 . In practice, magnetic fields of any magnet exhibit a spatial variation around the intended value B_0 , with which proton spins at different locations precess at different Larmor frequencies, growing rapidly out of phase. Consequently, the damping of $V(t)$ is hastened with a new characteristic time T_2^* that is smaller than T_2 . This faster, spurious T_2^* -damping overrides the T_2 -damping we wish to observe.

The field inhomogeneity causing the T_2^* -damping is spatially fixed and thus *deterministic*, while the T_2 -damping is caused by the *random* perturbations, i.e., spin–spin interactions and magnetic particle perturbations. This fundamental difference allows for techniques to recover T_2 despite the T_2^* -damping. Fig. 6 shows one such technique (Carr–Purcell technique). First, the RF magnetic field is applied for a duration of T_{90° (Eq. (3)) so that \vec{M} is tipped away from the z -axis onto the xy -plane [①]. The $x'y'$ -frame of Fig. 6 is a frame rotating about z -axis in the same sense as the spin precessions and at the same rate as the nominal precession frequency, i.e., the Larmor frequency at B_0 where the static field has spatial variations around. This rotating frame removes the nominal-frequency precession. In the rotating frame, during the RF excitation for T_{90° (90° pulse), \vec{M} exhibits a simple downward motion, instead of the spiraling downward motion of the laboratory frame; \vec{M} is rotated around x' -axis¹ by 90° to the positive y' -direction. Due to the field inhomogeneity, precessions of individual spins with differing Larmor frequencies dephase rapidly, dampening $V(t)$ with T_2^* time [②]; spins precessing faster (labeled '+') move clockwise (when looked from the positive z -axis), while slower spins ('-') move counterclockwise. After a while ($t = \tau$), a 180° -pulse is applied to rotate the spins again around x' -axis by 180°

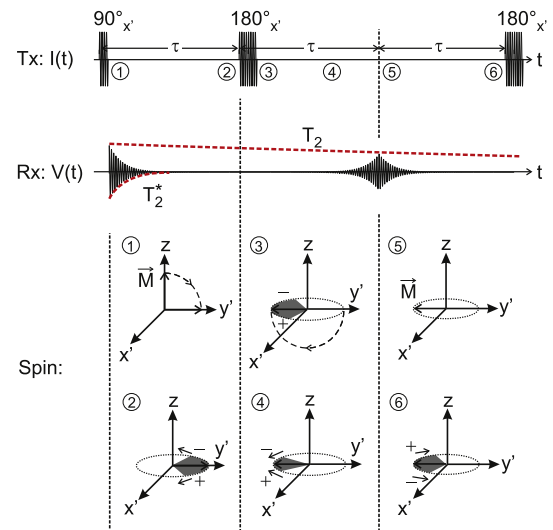


Fig. 6. Carr–Purcell pulse sequence.

[③], placing them now around the negative y' -axis. Faster (slower) spins still continue to move clockwise (counterclockwise), but due to the 180° flip, spins now re-phase [④], and $V(t)$ re-emerges, or 'echoes'. At $t = 2\tau$, the re-phasing becomes maximal, yielding \vec{M} unaffected by the field inhomogeneity and a locally maximal $V(t)$ [⑤]. After this, faster (slower) spins continue to rotate clockwise (counterclockwise), again causing T_2^* -damping. Applying another 180° -pulse will subsequently cause another echo to appear. Continued applications of 180° -pulses produce a sequence of echoes. As the random dephasing is not countered, T_2 -damping continues to progress in the background, and the envelope of the echoes decays with T_2 . In this way, T_2 can be measured.

The RF magnetic fields in excitation pulses can be inaccurate, causing errors in the rotation angles. As the angle errors accumulate, the envelope of the echoes decay faster than T_2 . This problem is solved (Fig. 7; Carr–Purcell–Meiboom–Gill (CPMG) method) by executing the 180° rotations about the y' -axis, instead of the x' -axis (as mentioned shortly before in the footnote, the axis of rotation can be chosen by controlling the phase of the excitation signal). In this way, if an angle error is introduced by the first 180° rotation, it is removed by the second 180° rotation.

¹ This axis for the θ -changing rotation due to the RF excitation is set by the initial phase of the RF excitation.

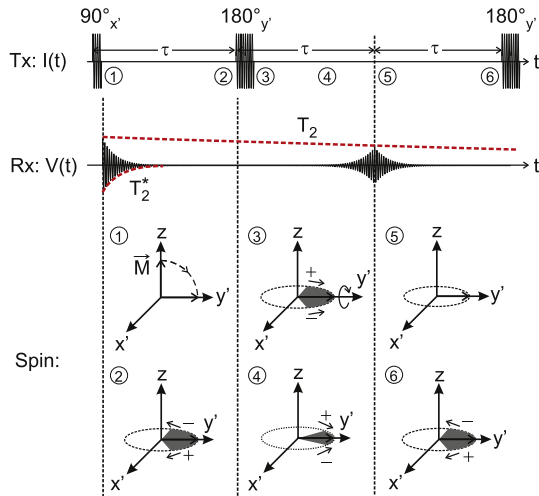


Fig. 7. Carr–Purcell–Meiboom–Gill pulse sequence.

2.6. Signal-to-noise ratio

The amplitude of $V(t)$ electromagnetically induced by the precession of \vec{M} is proportional to \vec{M} 's magnitude $M_0 \sim NB_0$ (Eq. (1)) and its precession frequency $\omega_0 = \gamma B_0$. In addition, the geometric configuration of the coil determines how effectively $V(t)$ is induced by the precession of \vec{M} ; by resorting to reciprocity, this effectiveness can be measured by how much RF magnetic field magnitude B_1 is produced by an RF excitation current amplitude I_1 , i.e., B_1/I_1 [17,18]. Overall, the amplitude of $V(t)$ is proportional to $N \cdot B_0^2 \cdot B_1/I_1$. The signal-to-noise ratio at the output of the receiver is then proportional to

$$\text{SNR} \propto \frac{N \cdot B_0^2 \cdot B_1/I_1}{F \sqrt{4kTR\Delta f}}, \quad (4)$$

where $4kTR\Delta f$ is the coil thermal noise (R : coil resistance) over the receiver bandwidth Δf , and F is the receiver noise figure in linear scale, which accounts for the receiver noise itself. The signal-to-noise ratio is proportional to B_0^2 . The small permanent magnets in our systems produce a relatively low field of ~ 0.5 T, which starts adding a challenge.

A much more significant challenge arises from the static field inhomogeneity, which is typically more pronounced with the smaller magnets, as in our case. With the field inhomogeneity, Larmor frequencies exhibit spatial variations across the sample. The 90° RF pulse has frequency components around $\omega_0 = \gamma B_0$ due to its finite duration of T_{90° , with the bandwidth $\sim 1/T_{90^\circ}$. The RF pulse then can excite only those spins in the region whose Larmor frequencies fall within the bandwidth. With significant static field inhomogeneity, the excitable region is reduced, decreasing the effective number of participant spins, N , in Eq. (4), leading to a substantially decreased signal-to-noise ratio. An excitation pulse with a shorter duration T_{90° can increase the excitable region, but this requires a larger B_1 (Eq. (3)) or a larger transmitted power, which is typically limited by electronics. In our systems using the small magnets with pronounced magnetic field inhomogeneity, we counter the reduction of the signal-to-noise ratio due to the decreased effective N , by minimizing the noise figure F and also by minimizing the receiver bandwidth Δf (Eq. (4)).

3. Miniature NMR system – 1st Prototype

Our 1st miniature NMR system (Fig. 1) [1,2], which weighs 2 kg, employs a $B_0 \sim 0.5$ -T, 1.25-kg magnet. The Larmor frequency $\omega_0/$

(2π) is ~ 21.3 MHz. The field inhomogeneity $\Delta B_0/B_0$ at the center of the magnet is about 50 ppm over a $5 \mu\text{L}$ volume. The 500-nH planar copper microcoil is in-house fabricated on a glass substrate [10], where the electroplated copper is $\sim 15 \mu\text{m}$ thick, with which $Q \sim 16$ at the Larmor frequency. A $5 \mu\text{L}$ sample is held on the microcoil with a $5 \mu\text{m}$ -thick passivation layer in between, inside a microfluidic container fabricated on top [10].

3.1. RF transceiver IC architecture

Fig. 8 shows the architecture of the RF transceiver used in this NMR system. The receiver path is in the lower portion. A weak spin-echo signal whose maximum available power is 0.5 fW appears at the front-end node 2°. In the frequency domain, the spin-echo signal is centered at the Larmor frequency with the bandwidth of $1/T_2^* \sim \gamma \Delta B_0/(2\pi) \sim 1.1 \text{ kHz}$. The signal is amplified by a low noise amplifier (LNA) and a variable-gain amplifier (VGA), and then is down-converted using mixers and quadrature local oscillator signals ('I' and 'Q') with frequency $\omega_0 + \delta$. We select $\delta/(2\pi) = 3 \text{ kHz}$, which is high enough to prevent swamping by $1/f$ noise, and is low enough to facilitate the rejection of the out-of-band noise with a bandpass filter with a moderate quality factor. The image noise is rejected by a digital-domain algorithm employing a Hilbert transformer.

The transmitter path is in the upper portion of Fig. 8. The excitation RF magnetic field is produced by the same quadrature local oscillators used in the receiver. Their frequency, $\omega_0 + \delta$, deviates from ω_0 , but the transmitted 90° and 180° pulses are windowed sinusoids with bandwidths of 15 kHz and 7.5 kHz, thus, they can still excite the entire sample, across which the Larmor frequency has a variation of $\gamma \Delta B_0/(2\pi) = 1.1 \text{ kHz}$. By gating the quadrature oscillator signals with the digital pulse generator, we produce the CPMG pulse sequence. The power amplifier (PA) is implemented off chip.

3.2. Receiver LNA and noise matching

The LNA is of common-source configuration (Fig. 9a). Since the Larmor frequency is smaller than the $1/f$ noise corner ($\sim 50 \text{ MHz}$) of NMOS transistors in the $0.18 \mu\text{m}$ CMOS technology used, PMOS devices \mathbf{M}_1 and \mathbf{M}_2 with smaller $1/f$ noise corner ($\sim 1 \text{ MHz}$) are used as input transistors. These PMOS transistors are built in separate N-wells, thus, they also help isolate the LNA from substrate noise produced by the transmitter. The coupling of the local oscillator signal into the LNA input is suppressed by cascoding (transistors $\mathbf{M}_3, \mathbf{M}_4$). With active load \mathbf{M}_5 and \mathbf{M}_6 , the LNA achieves a high voltage gain of 41 dB. A common-mode feedback circuit (CMFB) (Fig. 9b) ensures a correct output common mode in the LNA; the CMFB compares the output common-mode voltage V_{cmo} to $V_{bias,3}$, and its output V_{cmfb} is used to drive the gates of transistors \mathbf{M}_5 and \mathbf{M}_6 . The Miller capacitor C_3 and resistor R_3 are for frequency compensation.

Channel thermal noise of transistors is dominant noise source. The calculated input referred noise of the LNA is:

$$\frac{v_{n,LNA}^2}{\Delta f} \approx \frac{8kT\gamma_n}{g_{m1}} \left(1 + \frac{g_{m5}}{g_{m1}} \right), \quad (5)$$

where g_m denotes transistor transconductance and γ_n denotes transistor channel thermal noise coefficient. Here we have ignored the noise of transistors $\mathbf{M}_3, \mathbf{M}_4$, and the CMFB circuit (and the input-referred current noise of the LNA is negligible at the Larmor frequency). To minimize the $1/g_{m1}$ factor, a large tail current (4 mA) and wide input transistors ($900 \mu\text{m}$) are used. To minimize the g_{m5}/g_{m1} term, transistors \mathbf{M}_5 and \mathbf{M}_6 are made much narrower than transistors \mathbf{M}_1 and \mathbf{M}_2 . Subsequently, \mathbf{M}_5 and \mathbf{M}_6 need a large V_{GS} ,

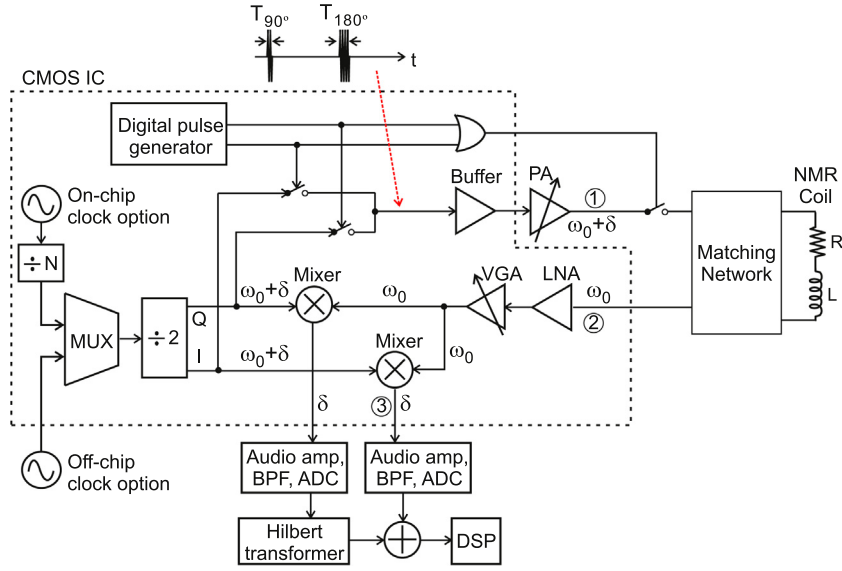


Fig. 8. RF transceiver in the first miniature NMR prototype (figure adapted from [1,2]).

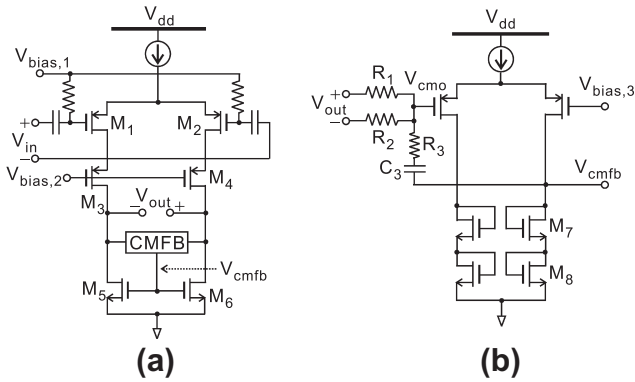


Fig. 9. (a) LNA and (b) CMFB.

which is provided by stacking transistors **M**₇ and **M**₈ in the CMFB (Fig. 9b). In this way the input-referred noise of the LNA is minimized. The measured input-referred noise of the entire receiver is 1.8 nV/√Hz, which is primarily contributed by the LNA.

Ultimately, we seek to minimize the receiver noise figure *F*, for which not only the input-referred noise minimization, but also the optimal LNA-coil matching plays a crucial role. Consider a general passive network between the coil and the LNA, whose voltage

transfer function from the coil side to the amplifier side assumes a value of α at the Larmor frequency. This is shown in Fig. 10a along with the NMR signal $V(t)$'s rms value, V_{rms} , coil's thermal noise $\overline{v_{n,R}^2} = 4kTR\Delta f$ over the signal bandwidth Δf , and the LNA's input referred voltage noise $\overline{v_{n,LNA}^2}$ also over the signal bandwidth. With the voltage gain α in the matching network, noise figure *F* of the LNA is given by

$$F = \frac{SNR_{in}}{SNR_{out}} = \frac{V_{rms}/(\overline{v_{n,R}^2})^{1/2}}{\alpha V_{rms}/(\alpha^2 \overline{v_{n,R}^2} + \overline{v_{n,LNA}^2})^{1/2}} = \left(1 + \frac{\overline{v_{n,LNA}^2}/\Delta f}{\alpha^2 \cdot 4kTR}\right)^{1/2}, \quad (6)$$

where we have neglected the noise of the passive network, which we will shortly justify. From Eq. (6), it is clear that in addition to the small input-referred noise of the LNA, a larger voltage gain α helps lowering *F*. To attain a large value of α , we use a single shunt capacitor *C* as the passive network (Fig. 10b), and the *C* value is chosen in such a way that it resonates with the coil inductor at the Larmor frequency. In this way, a large value of α is obtained, specifically: $\alpha = \sqrt{Q^2 + 1} \approx 16$. Note that this resonant noise matching leads to impedance mismatch between the LNA and the coil. At the Larmor frequency, capacitors are far less lossy than the coil, which justifies the omission of the noise of the passive network in writing Eq. (6). The large value of α due to the resonance noise matching together with the minimized input-referred noise of the LNA significantly reduces *F*, whose measured value is 0.7 dB.

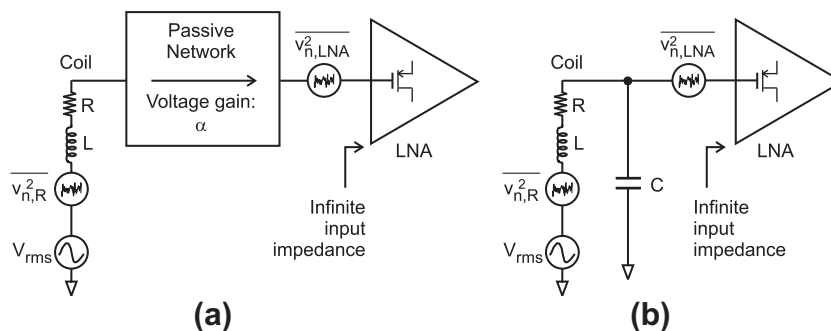


Fig. 10. Coil-LNA noise matching.

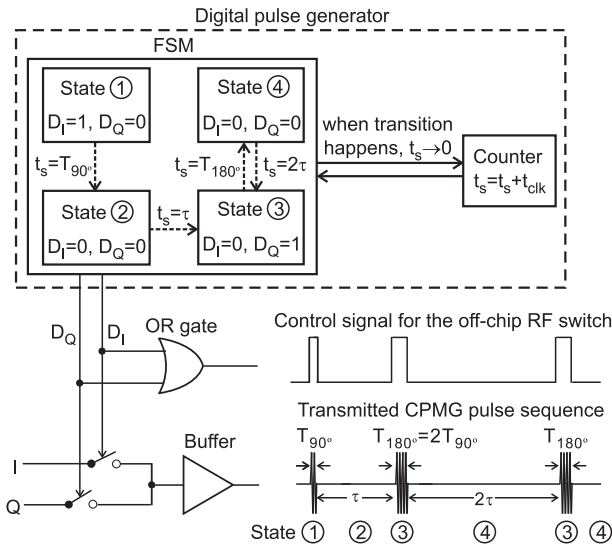


Fig. 11. Block diagram of the digital pulse generator.

3.3. Digital pulse generator

The CPMG pulse sequence is obtained by using one of the two quadrature oscillator signals for the 90° pulse, and the other quadrature oscillator signal for the 180° pulses. The axes of rotation for \vec{M} in the rotating frame corresponding to the two quadrature signals are perpendicular, thus the CPMG sequence is obtained (Fig. 7). The arrangement to gate the two quadrature oscillator signals in the transmitter to obtain the CPMG pulse sequence is shown in Fig. 8, and is detailed in Fig. 11. A finite-state-machine (FSM) and a counter are used. The counter output, t_s , is reset to 0 whenever the FSM transits between its internal states. Thus, t_s represents how long the FSM stays at its present state, and is used to control its state transition. The FSM's two outputs D_I and D_Q gate the quadrature signals 'I' and 'Q' to produce the CPMG pulse sequence. D_I and D_Q also feed an OR-gate, which controls the off-chip

switch between the coil and the PA (Fig. 8). The FSM deals with 4 states, ①, ②, ③ and ④, which respectively represent the time duration of the 90° pulse, the time interval between the 90° pulse and the first 180° pulse, the time duration corresponding to any 180° pulse, and the time duration between any two adjacent 180° pulses. The FSM starts from state ①, and sequentially moves to states ②, ③, and ④ when t_s accumulates to the corresponding values. Then the FSM goes back and forth between states ③ and ④ to repeat the 180° pulses.

4. Miniature NMR systems – 2nd and 3rd prototypes

The 2nd prototype (Fig. 2) [3,4] uses the same magnet as the 1st prototype (Larmor frequency: ~21.3 MHz), but integrates the planar microcoil in the same RF transceiver IC for lab-on-a-chip operation. Due to thin metals, the 430-nH integrated microcoil has a Q of 1.9, even after connecting 5 metal layers in parallel; this low Q is due mainly to the coil's dc resistance, while the substrate and skin effect are negligible at the Larmor frequency. The chip is packaged with the coil part exposed and the rest encapsulated. This open package provides an effective container on top of the coil to hold a 5 μ L sample, while the sample is separated from the coil by the passivation layer native to the CMOS process. To cope with the signal-to-noise ratio reduction due to the lossy coil, the RF transceiver was redesigned. Also its integration level was increased, incorporating a power amplifier (PA) on chip. The transceiver architecture is shown in Fig. 12. The dashed lines show the integration boundary, which includes the coil, capacitor C_m for resonant noise matching, and transceiver front-end except the local oscillator source. The mixer outputs feed the off-chip back-end signal processing unit.

The integrated PA is a differential chain of inverters that are quadrupled in size to amplify power and ensure the output drivability (Fig. 12). The output amplitude of this class-D PA is fixed at V_{DD} , while tuning the output power is necessary to control the 90° and 180° pulse durations (e.g., see Eq. (3) for the 90° pulse). For power tuning, we vary the duty cycle of the transmitted signal: the signal power at the Larmor frequency is maximal for the duty

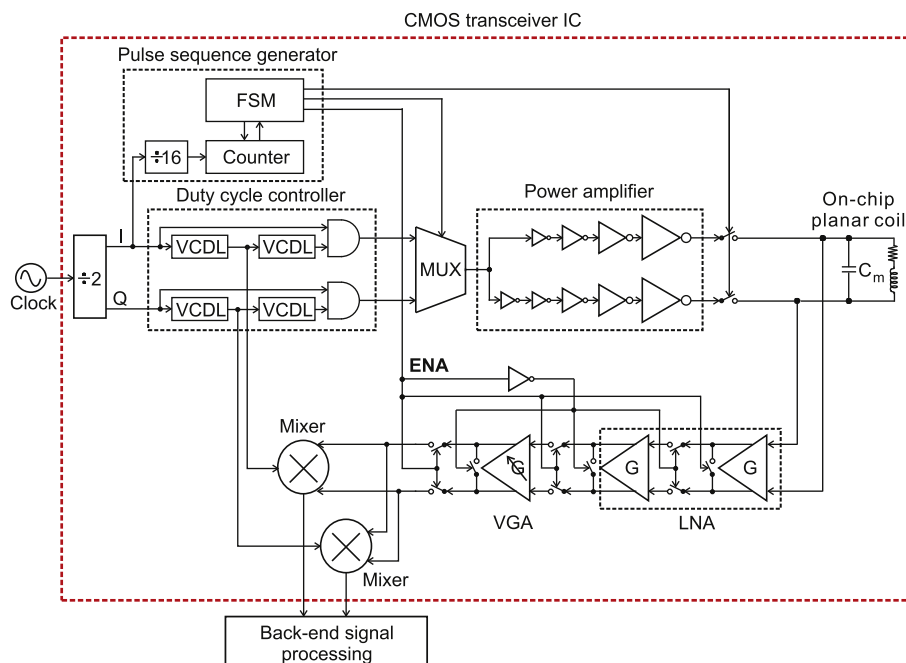


Fig. 12. CMOS RF transceiver for the 2nd NMR prototype (figure adapted from [3,4]).

cycle of 50%, and is 0 for the duty cycle of 0%. Other harmonic components of the output signal will be irrelevant, as they cannot excite the proton spins; that is, this scheme exploits the natural high- Q filtering ability of the proton spin in the static magnetic field. The duty cycle is tuned by using voltage-controlled delay lines (VCDLs) and logic gates. The receiver is a revision from the 1st prototype to further reduce the input-referred noise, e.g.,: the active loads are replaced by resistive loads; the CMFB thus is removed; and two stages are cascaded to compensate for the reduced gain due to the resistive loads. The measured input-referred noise of the entire receiver is $1.26 \text{ nV}/\sqrt{\text{Hz}}$, which is 30% less than that of the first prototype. The measured noise figure is 2.2 dB, which is larger than that of the first prototype; this is because the voltage gain $\alpha = \sqrt{Q^2 + 1}$ of the noise matching network has been substantially reduced in this second prototype. The measured output impedance of the differential PA is 27Ω . The duty cycle can be tuned from 0% to 45%, which translates to the output power tuning from 0 to 80 mW.

The 3rd prototype (Fig. 3) [3,4], which employs an even smaller, 70-g, 0.56-T magnet (Larmor frequency: $\sim 23.9 \text{ MHz}$), weighs only 0.1 kg. The magnet has a cylindrical shape with a height of 2.3 cm and a base diameter of 2.5 cm. This small magnet has a significant magnetic field inhomogeneity of 500 ppm over a $2 \mu\text{L}$ volume, inevitably reducing the NMR signal strength. To counter this, we use a 100-nH solenoidal microcoil with a Q of 28. The coil is wound around a capillary tube in which a $2\text{-}\mu\text{L}$ sample is placed. The RF transceiver used in this prototype shares almost the same design as that in the 2nd prototype, except that the coil and the matching capacitor are not integrated. The measured receiver noise figure is 0.9 dB.

5. NMR and biomolecular sensing experiments

Fig. 13 shows the measurements of the down-converted ^1H NMR signal using the 3rd prototype with a water sample. The repeated ringings are spin echo responses to the CPMG pulse sequence. $T_2 = 100 \text{ ms}$ is extracted from the exponentially decaying envelope of the spin echoes. The repeated spikes between the echoes are due to the coupling of the large excitation pulses.

The miniature NMR systems detected a range of biological molecules and compounds [1–4]. For example, Fig. 14 shows the detection of avidin using the 3rd prototype. Magnetic particles (diameter: 38 nm) coated with biotins are introduced into a water sample. In the absence of avidin, the particles stay mono dispersed, yielding T_2 of 48 ms. In the presence of avidin, the biotinylated magnetic particles bind to avidin, forming clusters [9] and reducing T_2 to 40 ms. The 3rd prototype detected down to 1 avidin molecule in 600 million water molecules.

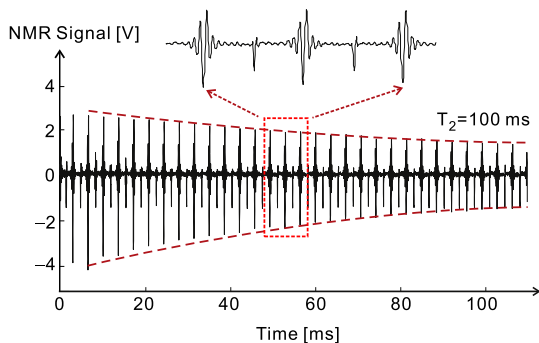


Fig. 13. Down-converted ^1H NMR signal measured with the 3rd prototype (figure adapted from [3,4]).

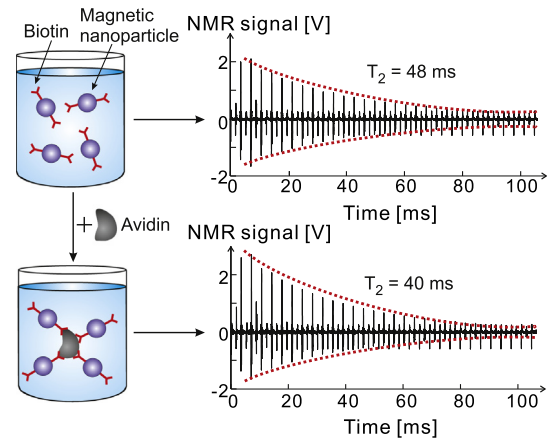


Fig. 14. Avidin detection with the 3rd prototype (figure adapted from [3,4]).

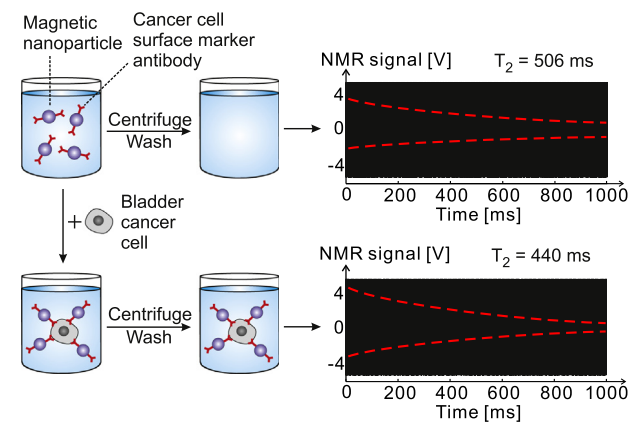


Fig. 15. Human bladder cancer cell detection with the 2nd prototype (figure adapted from [3,4]).

Yet another example, now with the 2nd prototype, is the detection of human bladder cancer cells (Fig. 15). Magnetic particles (diameter: 40 nm) coated with monoclonal antibody to bladder cancer cell surface markers are introduced into a water sample. In the absence of cancer cells, the magnetic particles are mono dispersed, but in the presence of the cancer cells, magnetic particles bind to the cell surface. In the latter sample, centrifugation [19] separates the cells and unattached magnetic particles, and the unattached particles are washed away. The T_2 time difference is evident (Fig. 15). The system detects down to ~ 18 cells per μL .

6. Conclusion and outlook

We reviewed our recent developments of small NMR biomolecular sensors [1–4]. The miniaturization was made possible by using small-sized, low-quality magnets, and by designing high-performance integrated RF transceivers that counter the effect of the low-quality magnets. The work involved a repertoire of technical areas, ranging from integrated circuits to biomolecular detection to the science and technology of NMR.

This work can be put in the general context of the research efforts to interface solid-state electronic chips with biological systems to provide bioanalytical capabilities [20–31]. The electronic and biological systems interfaces utilize spin-based magnetic interactions as in this reviewed work, or charge-based electric interactions as in the ion-sensitive field-effect transistors [20–25], while more complex coupling modalities, such as

electronics-regime plasmonic interactions [32–34], may be made available in the future. While optics-based bioanalytical systems will continue to be used broadly into the foreseeable future, the solid-state electronic and bio systems interfaces have attractive features such as low cost, chip-scale operation, massive parallelism, and accessibility. There thus are continuing efforts to develop a host of such interfaces. Our NMR biomolecular sensors add to the list.

From the circuit engineering point of view, the solid-state electronic and bio systems interfaces create needs for a range of application-specific integrated circuits. For example, our NMR work reviewed here showcases how RF integrated circuits can be used not only for their prevalent wireless applications, but also for biomolecular detection aimed at medical diagnostics. For another example, integrated temperature sensors [35,36] will become important in systems interfaced with living organisms or *ex vivo* biological tissues, where monitoring and controlling temperature of the electronic chip is important not to damage these biological systems. For implanted, *in vivo*, or field-use applications, low-power design of analog and mixed-signal circuits will be important; digitally-assisted design techniques [37,38] that have been an important design trend may prove especially useful for these applications.

The CMOS NMR systems and their biomolecular detection applications we reviewed in this paper are focused on the measurements of relaxation times, limited by the field inhomogeneity of the specific small magnets used. The application scope of the small NMR systems will be significantly broadened, if their capability can be expanded into the realm of high-resolution spectroscopy. This suggests another interesting future research path.

References

- [1] Liu Y, Sun N, Lee H, Weissleder R, Ham D. CMOS mini nuclear magnetic resonance system and its application for biomolecular sensing. In: Digest of technical papers. IEEE international solid-state circuits conference; February 2008. p. 140–1.
- [2] Sun N, Liu Y, Lee H, Weissleder R, Ham D. CMOS RF biosensor utilizing nuclear magnetic resonance. IEEE J Solid-State Circ 2009;44:1629–43.
- [3] Sun N, Yoon T-J, Lee H, Andress W, Demas V, Prado P, et al. Palm NMR and one-chip NMR. In: Digest of technical papers. IEEE international solid-state circuits conference; February 2010. p. 488–9.
- [4] Sun N, Yoon T-J, Lee H, Andress W, Weissleder R, Ham D. Palm NMR and one-chip NMR. IEEE J Solid-State Circ 2011;46:342–52.
- [5] Slichter JA. Principles of magnetic resonance. Heidelberg, (Germany): Springer-Verlag; 1992.
- [6] Canet D. Nuclear magnetic resonance: concepts and methods. NY: Wiley; 1996.
- [7] Gunther H. NMR spectroscopy: basic principles, concepts, and applications in chemistry. Wiley; 1995.
- [8] Brown MA, Semelka RC. MRI: basic principles and applications. Wiley-Blackwell; 2010.
- [9] Perez JM, Josephson L, O'Loughlin T, Hoegeman D, Weissleder R. Magnetic relaxation switches capable of sensing molecular interactions. Nat Biotechnol 2002;20:816–20.
- [10] Lee H, Sun E, Ham D, Weissleder R. Chip-NMR biosensor for detection & molecular analysis of cells. Nat Med 2008;14:869–74.
- [11] Sun B, Dunn K-J. A global inversion method for multi-dimensional NMR logging. J Magn Reson 2005;172:152–60.
- [12] Charlton AJ, Farrington WHH, Brereton P. Application of ¹H NMR and multivariate statistics for screening complex mixtures: quality control and authenticity of instant coffee. J Agric Food Chem 2002;50:3098–103.
- [13] <http://www.bruckeroptics.com/minispec.html>.
- [14] Ham D, Hajimiri A. Virtual damping and Einstein relation in oscillators. IEEE J Solid-State Circ 2003;38:407–18.
- [15] Li X, Yildirim OO, Zhu W, Ham D. Phase noise of distributed oscillators. IEEE Trans Microw Theor Tech 2010;58(8):2105–17.
- [16] Li X, Zhu W, Ham D. Phase diffusion and Lamb-shift-like spectrum shift in classical oscillators; 2010. arXiv:0908.2214.
- [17] Hoult D. The NMR receiver: a description and analysis of design. Prog Nucl Magn Reson Spectrosc 1978;12:41–77.
- [18] Hoult DI, Richards RE. The signal-to-noise ratio of the nuclear magnetic resonance experiment. J Magn Reson 1976;24:71–85.
- [19] Lee H, Yoon T-J, Figueiredo J-L, Swirski FK, Weissleder R. Rapid detection and profiling of cancer cells in fine-needle aspirates. Proc Natl Acad Sci 2009;106:12459–64.
- [20] Bergveld P. The future of biosensors. Sens Actuat A 1996;56:65–73.
- [21] Rothberg JM et al. An integrated semiconductor device enabling non-optical genome sequencing. Nature 2011;475:348–52.
- [22] Bausells J, Carrabina J, Errachid A, Merlos A. Ion-sensitive field-effect transistors fabricated in a commercial CMOS technology. Sens Actuat B Chem 1999;57:56–62.
- [23] Milgrew M, Hammond P, Cumming D. The development of scalable sensor arrays using standard CMOS technology. Sens Actuat B Chem 2004;103:37–42.
- [24] Patolsky F, Timko B, Zheng G, Lieber CM. Nanowire-based nano-electronic devices in the life sciences. MRS Bull 2007;32:142–9.
- [25] Patolsky F, Zheng G, Hayden O, Lakadamyali M, Zhuang X, Lieber CM. Electrical detection of single viruses. Proc Natl Acad Sci 2004;101:14017–22.
- [26] Sun N, Liu Y, Qin L, Xu G, Ham D. Solid-state and biological systems interface. In: European solid-state device research conference & european solid-state circuits conference (joint paper); September 2012. p. 14–7.
- [27] Ham D, Westervelt RM. The silicon that moves and feels small living things. IEEE Solid State Circ Soc Newslett 2007;12:4–9.
- [28] Lee H, Ham D, Westervelt RM, editors. CMOS biotechnology. Springer; 2007.
- [29] Lee H, Liu Y, Westervelt RM, Ham D. IC/microfluidic hybrid system for magnetic manipulation of biological cells. IEEE J Solid-State Circ 2006;41(6):1471–80.
- [30] Lee H, Liu Y, Alsberg E, Ingber DE, Westervelt RM, Ham D. An IC/microfluidic hybrid microsystem for 2D manipulation of individual biological cells. In: Digest of technical papers. IEEE international solid-state circuits conference; February 2005. p. 80–1.
- [31] Lee H, Liu Y, Ham D, Westervelt RM. Integrated cell manipulation system – CMOS/microfluidic hybrid. Lab Chip 2007;7:331–7.
- [32] Yoon H, Yeung KYM, Umansky V, Ham D. A Newtonian approach to extraordinarily strong negative refraction. Nature 2012;488:65–9.
- [33] Andress W, Yoon H, Yeung KYM, Qin L, West K, Pfeiffer L, et al. Ultra-subwavelength two-dimensional plasmonic circuits. Nano Lett 2012;12:2272–7.
- [34] Yeung KYM, Yoon H, Andress W, West K, Pfeiffer L, Ham D. Two-path solid-state interferometry using ultra-subwavelength two-dimensional plasmonic waves. Appl Phys Lett 2013;102:021104.
- [35] Ha D, Woo K, Meninger S, Xanthopoulos T, Crain E, Ham D. Time-domain CMOS temperature sensors with dual delay-locked loops for microprocessor thermal monitoring. IEEE Trans VLSI Syst 2012;20:1590–601.
- [36] Woo K, Meninger S, Xanthopoulos T, Crain E, Ha D, Ham D. Dual-DLL-based CMOS all-digital temperature sensor for microprocessor thermal monitoring. In: Digest of technical papers. IEEE international solid-state circuits conference; 2009. p. 68–9.
- [37] Sun N, Lee HS, Ham D. A 2.9-mW 11-b 20-MS/s pipelined ADC with dual-mode-based digital background calibration. In: European solid-state circuits conference; 2012. p. 269–72.
- [38] Sun N, Lee HS, Ham D. Digital background calibration in pipelined ADCs utilizing commutated feedback capacitor switching. IEEE Trans Circ Syst – II 2008;55:877–81.